

Journal of Biomedical Optics

SPIEDigitalLibrary.org/jbo

Network signatures of nuclear and cytoplasmic density alterations in a model of pre and postmetastatic colorectal cancer

Dhwanil Damania
Hariharan Subramanian
Vadim Backman
Eric C. Anderson
Melissa H. Wong
Owen J. T. McCarty
Kevin G. Phillips



Network signatures of nuclear and cytoplasmic density alterations in a model of pre and postmetastatic colorectal cancer

Dhwanil Damania,^a Hariharan Subramanian,^a Vadim Backman,^a Eric C. Anderson,^b Melissa H. Wong,^{b,c,d} Owen J. T. McCarty,^{b,c,e} and Kevin G. Phillips^{d,e,*}

^aNorthwestern University, Biomedical Engineering Department, Evanston, Illinois 60208

^bOregon Health & Science University, Knight Cancer Institute, Portland, Oregon 97239

^cOregon Health & Science University, School of Medicine, Department of Cell & Developmental Biology, Portland, Oregon 97239

^dOregon Health & Science University, School of Medicine, Department of Dermatology, Portland, Oregon 97239

^eOregon Health & Science University, School of Medicine, Department of Biomedical Engineering, Portland, Oregon 97239

Abstract. Cells contributing to the pathogenesis of cancer possess cytoplasmic and nuclear structural alterations that accompany their aberrant genetic, epigenetic, and molecular perturbations. Although it is known that architectural changes in primary and metastatic tumor cells can be quantified through variations in cellular density at the nanometer and micrometer spatial scales, the interdependent relationships among nuclear and cytoplasmic density as a function of tumorigenic potential has not been thoroughly investigated. We present a combined optical approach utilizing quantitative phase microscopy and partial wave spectroscopic microscopy to perform parallel structural characterizations of cellular architecture. Using the isogenic SW480 and SW620 cell lines as a model of pre and postmetastatic transition in colorectal cancer, we demonstrate that nuclear and cytoplasmic nanoscale disorder, micron-scale dry mass content, mean dry mass density, and shape metrics of the dry mass density histogram are uniquely correlated within and across different cellular compartments for a given cell type. The correlations of these physical parameters can be interpreted as networks whose nodal importance and level of connection independence differ according to disease stage. This work demonstrates how optically derived biophysical parameters are linked within and across different cellular compartments during the architectural orchestration of the metastatic phenotype. © 2014 Society of Photo-Optical Instrumentation Engineers (SPIE) [DOI: 10.1117/1.JBO.19.1.016016]

Keywords: colorectal cancer; cancer cell lines; quantitative phase microscopy; partial wave spectroscopic microscopy; disorder strength; cell density; subcellular architecture; label-free optical microscopy.

Paper 130686RR received Sep. 20, 2013; revised manuscript received Dec. 6, 2013; accepted for publication Dec. 13, 2013; published online Jan. 20, 2014.

1 Introduction

Although major advances have been made in the screening and treatment of colorectal cancer (CRC), it remains the second deadliest form of cancer in the United States with nearly 150,000 cases and 50,000 deaths annually.¹ CRC has a 5-year survival rate of 64% with the stage of the disease at the time of diagnosis being the key regulator of survival: 19% of CRC patients are diagnosed with an advanced staging of the disease, decreasing their overall survival rate to only 11%.² These poor outcomes demonstrate the need for improved accessibility and reliability for early-stage diagnosis of CRC. To address the clinical need for earlier-stage diagnosis of CRC, and cancer in general, efforts are underway to establish physical sciences-based diagnostic signatures of cells and tissues altered during the pathogenesis of cancer.³

Cytoplasmic and nuclear density alterations accompany aberrant genetic, epigenetic, and molecular perturbations in cells contributing to the pathogenesis of cancer. Architectural changes in primary and metastatic tumor cells can be optically quantified at the nanometer and micrometer spatial scales through label-free imaging and sensing modalities. Central to these techniques are theories that link biological structure to

experimentally controlled electromagnetic wave interactions. These strategies include light scattering spectroscopy,^{4,5} angle-resolved low coherence interferometry,^{6,7} Raman spectroscopy,^{8,9} diffuse optical spectroscopy,¹⁰ partial wave spectroscopic (PWS) microscopy,^{11,12} low-coherence enhanced backscattering,^{12,13} quantitative phase microscopy,^{14–16} and non-interferometric quantitative phase microscopy (NIQPM).¹⁷ Cellular level observations of cancerous cells enabled by these technologies include an increase in subcellular constituent size,^{4,5,7,13,14,17,18} changes in density,^{7,14,17,18} alterations of the organization of this density to a more inhomogeneous state,^{12,14,18} alterations in cellular metabolism,¹⁰ and changes in biochemical composition⁸ including higher concentrations of nuclear acids.⁹

To date, label-free optical studies undertaking a detailed analysis of cellular physical properties in the context of cancer have been focused on measuring single parameters to establish one-dimensional biophysical signatures of cellular and/or tissue alterations due to cancer. These efforts have been fruitful in translational studies of patient cohorts exploring detection of cancers prior to alterations of cells and tissues that can be detected by histology.^{12,19,20} These efforts represent a biophysical strategy to characterize cancer that can operate in tandem

*Address all correspondence to: Kevin Phillips, E-mail: phillkev@ohsu.edu

with assays to identify specific genomic and proteomic alterations in cancers.¹⁰

The methodological approach of large-scale genomic/proteomic array studies and systems biology has elucidated the utility of simultaneously determining correlations among many genes and proteins expressed in cancerous cells to reveal signaling network topologies, feedback loops, and heterogeneity in genomic/proteomic expression profiles underlying cancer.²¹ Such a network approach has yet to be utilized to quantify and visualize the inter-relationships of multiscale physical properties of cancer cells. Just as there is limited utility in relating any one gene or protein to the molecular origin of cancer, there is an increasing awareness that enhancing our understanding of the physical origins of cancer will rely on a multifaceted set of measurements to probe the parametric “phase space” of normal and pathological tissue function in contrast to focusing on any one parameter to explain the cancerous state.^{3,21} This methodology could potentially impact clinical care through the translation of new metrics that might bring about earlier detection and sensitive monitoring of disease.

Using a network approach as a quantitative guide, we hypothesized that cancer cells in the metastatic cascade not only possess distinct cytoplasmic and nuclear density properties as a function of tumorigenic potential but are also characterized by distinct correlations among these physical characteristics that define a network topology specific to disease stage.

To examine potential correlative structures among cellular density metrics in cells involved in the cellular level transition to a metastatic phenotype, we utilized morphologically similar isogenic (patient matched) SW480 (primary colon adenocarcinoma, early stage), and SW620 (lymph node metastasis, late stage) CRC cell lines.^{22, 23} Using a novel optical approach combining quantitative phase microscopy and PWS microscopy, we quantified nanoscale and microscale cellular density properties including nanoscale nuclear disorder strength, and at the micron scale: nuclear and cytoplasmic area, dry mass content, mean dry mass density, and shape metrics of the dry mass density histogram including the median, mode, min, max, skew, and kurtosis. Similar multiparameter approaches have been previously utilized to characterize phase distortions in tissue sections,¹⁴ red blood cells,²⁴ phase fluctuations observed in waves transmitted through cells,¹⁶ and in the context of monitoring the cell cycle through phase-derived parameters.²⁵ Our approach is the first to investigate the interdependence of these parameters.

In a model system of metastatic transition, we demonstrate that alterations in the nanoscale nuclear disorder strength are increased in cells with enhanced tumorigenic potential^{11,12} and, moreover, are positively correlated with increased nuclear density fluctuations at the micron scale. It is observed that micron-scale cytoplasmic and/or nuclear biophysical parameters across disease stage are not always significantly different; however, the interdependence of these density parameters, quantified through their level of correlation, provides a unique quantitative characterization of early- and late-stage disease. Specifically, these correlations define a physical parameter network topology specific to disease stage in this model system. Understanding the interdependence of subcellular properties provides new insight into how biophysical parameters are linked within and across different cellular compartments and across different spatial scales during the biophysical coordination of the cancer phenotype.

2 Materials and Methods

2.1 Cell Preparation

The patient-matched SW620 (lymph node metastasis, late stage) and SW480 (primary colon adenocarcinoma, early stage) CRC cell lines²² were obtained from American Type Cell Culture. Cells were cultured on Lab-Tek glass-bottomed chamber slides (Thermo Scientific, Waltham, Massachusetts) in Dulbecco’s modified Eagle’s medium containing 10% fetal bovine serum (Life Technologies, Carlsbad, California) and maintained in a controlled environment at 37°C with 5% CO₂/air atmosphere. Cells were fixed prior to imaging. Cells were prepared either for NIQPM or PWS imaging. For NIQPM imaging, a coverslip was mounted over the top of the cells using fluoromount G (refractive index = 1.4, Southern Biotech, Birmingham, Alabama). For PWS microscopy, cells were imaged in reflection mode on the chamber slides with no additional preparation.

2.2 Noninterferometric Quantitative Phase Microscopy

Cellular density was measured using NIQPM on an upright optical microscope (Axio Imager; Carl Zeiss, Gottingen, Germany) equipped with a $\times 63/1.4$ NA oil immersion objective and an air coupled condenser lens providing Köhler illumination with an adjustable NA ranging from 0.1 to 0.9. Through-focus bright field imagery of the cells was carried out using monochromatic light (540 ± 20 nm) generated by passing the light from a 100-W mercury lamp through an interference filter (Chroma Technology Corp., Bellows Falls, VT) and then a condenser lens set to NA = 0.1. Images of the cells were recorded with a charge-coupled device camera (AxioCam Mrc5 12-bit camera; Carl Zeiss, Gottingen, Germany) and Slidebook 5.5 software (Intelligent Imaging Innovations, Denver, CO). Through-focus images were acquired in 0.1- μm increments over a 10- μm axial range [Fig. 1(a)].

The principle of NIQPM and its application to quantifying the spatial cellular density map in a cell has been established and described elsewhere.^{15,17,26–30} Briefly, NIQPM consists of an image acquisition step and a postprocessing procedure to determine the phase profile of optical waves transmitted through the specimen. Through-focus intensity measurements [Fig. 2(a)] in different planes along the optical axis through the specimen are used to approximate the axial derivative of the intensity. A Green function technique,¹⁷ carried out using a custom written program in MATLAB (The MathWorks, Inc., Natick, MA), is then utilized to solve for phase using the transport of intensity equation, which defines the relationship of axial intensity variations to phase²⁶ under the paraxial approximation. Last, phase is used to determine the axially integrated mass density, ρ ($\text{pg}/\mu\text{m}^2$),^{31–34} from which the total cellular mass is determined by integration over the area of the cell [Fig. 2(b)]. The optimal phase profile is ensured by the generation of a pseudo differential interference contrast (DIC) image given by the spatial derivative of the phase along the -45 -deg line of the phase image [Fig. 2(c)].³⁵ The pseudo DIC image must recapitulate the true DIC image [Fig. 2(d)] in terms of focusing and structural elements such as nuclear envelope, nucleoli, and membrane protrusions of the cell [Figs. 2(c) and 2(d), arrows].

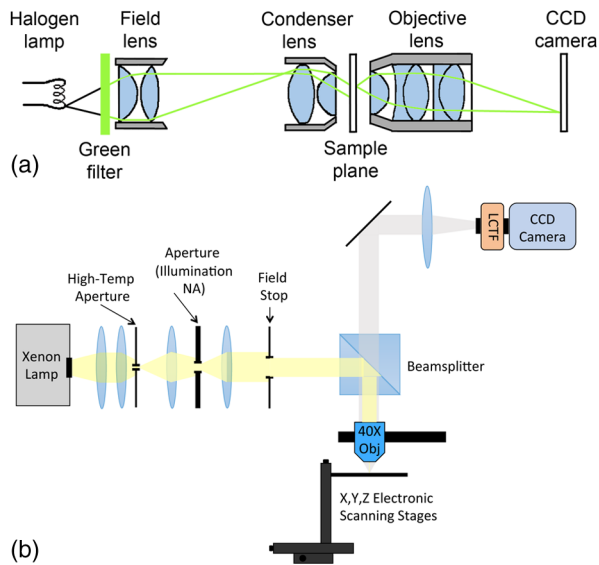


Fig. 1 Optical instrumentation. (a) Kohler-illuminated bright field microscopy. (b) Partial wave spectroscopic microscopy.

2.3 NIQPM Image Segmentation

To examine cellular dry mass density parameters across subcellular compartments, and across disease stage, projected mass density maps were segmented into nuclear and cytoplasmic domains. Subcellular domains were identified using DIC imagery to visualize the nuclear envelope of morphologically similar CRC cell types [Figs. 2(d) and 3(a)]. A binary mask was created for each region so that the density distribution in

each compartment could be isolated. Histograms of the *subcellular* density map were constructed with bin sizes of $0.01 \text{ (pg}/\mu\text{m}^2)$ over the range of 0 to $2 \text{ (pg}/\mu\text{m}^2)$ for the cytoplasm [Fig. 3(b)] and nucleus [Fig. 3(c)] of each cell. These histograms were then normalized into probability density functions for each cell type [Figs. 3(d) and 3(e)]. From the image segmentation and histogram procedures, 11 parameters were determined for each subcellular compartment: area, total mass, density mean, standard deviation, coefficient of variation, mode, median, min, max, skew, and kurtosis (Table 1). Twenty cells per CRC cell type were investigated.

2.4 PWS Microscopy

PWS microscopy measurements [Fig. 1(b)] were carried out on a second-generation instrument described in detail elsewhere.³⁶ Briefly, a plane wave of white light from a xenon lamp (150 W; Oriel, Stratford, CT) is produced by a 4f-lens relay system that focuses onto the sample plane by a low $\text{NA} = 0.2$ condenser lens. Light reflected by the specimen is collected by a $\text{NA} = 0.4$ objective lens (Edmund Optics, Barrington, NJ). The objective lens contains a correction collar to compensate for aberrations. The back propagating wavefronts are projected through a liquid crystal tunable filter (LCTF; CRI, Woburn, MA), with a spectral resolution, $\Delta\lambda = 7 \text{ nm}$, and spectral range of 400 to 700 nm. At each wavelength, the sample plane is imaged onto a CCD camera [Fig. 1(b)].

A three-dimensional data cube of the reflected intensity $I(\lambda, x, y)$ [where (x, y) refers to a specific pixel in the object plane and λ is the wavelength] is generated. We normalized the acquired spectra by the combined LCTF and CCD spectral

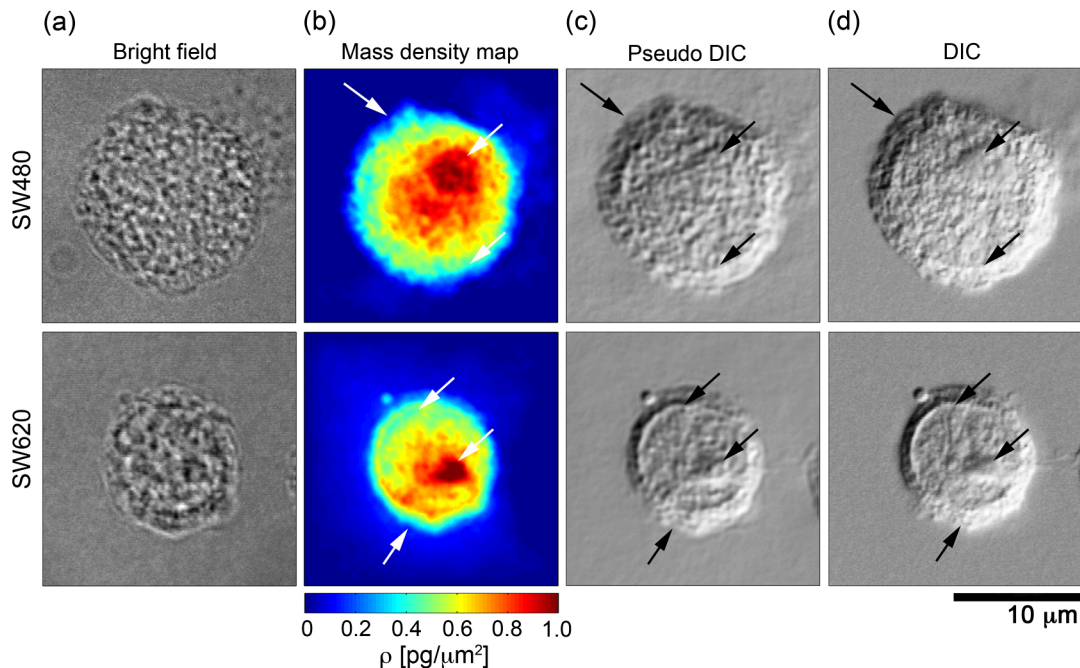


Fig. 2 Micron-scale density measurement of SW cell types using noninterferometric quantitative phase microscopy (NIQPM). (a) Bright field imagery of SW cells at the central focus of the image stack used in the NIQPM algorithm to determine axially integrated dry mass density. (b) Spatial maps of axially integrated dry mass density among cellular compartments in SW cells. (c) Pseudo DIC imagery generated by the spatial derivative of the phase profile of transmitted waves through the sample along the -45 -deg line of the phase image (not pictured). (d) True DIC imagery of the SW cells under $\text{NA} = 0.9$ Köhler illumination. Arrows denote membrane protrusions, nuclear envelope, and nucleoli common to both pseudo DIC and DIC imagery.

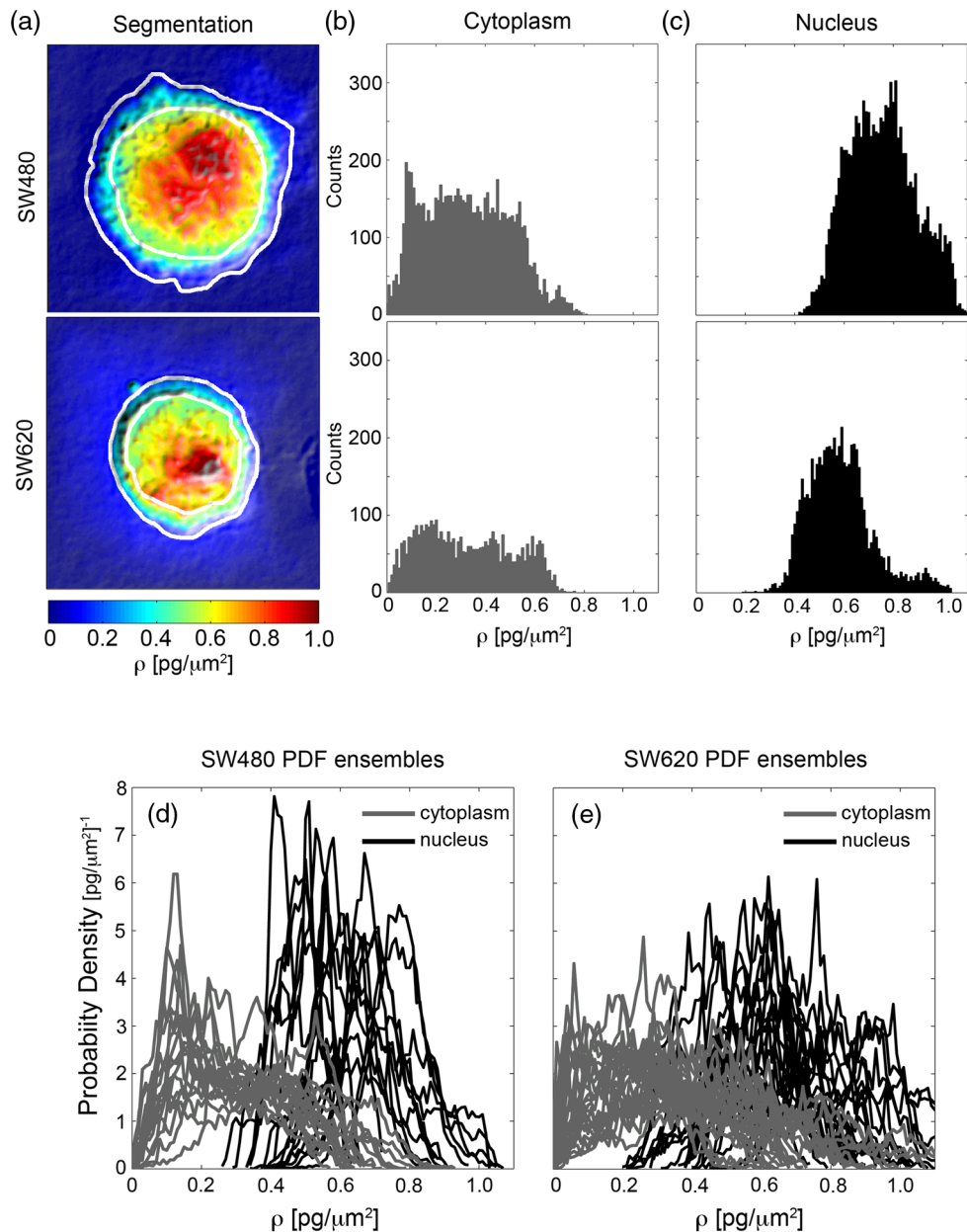


Fig. 3 Image segmentation of NIQPM-derived spatial density maps. (a) Overlay of DIC and mass density map. The nuclear envelope identified in DIC imagery of each cell type was used to create outlines of the nuclear and cytoplasmic regions in the dry mass density map of each cell. The dry mass density of the cytoplasm (b) and nucleus (c) are binned into histograms of bin size 0.01 over the range of 0 to 2 ($\text{pg}/\mu\text{m}^2$). Histograms are normalized into probability density functions (PDFs) for both compartments. (d) Ensemble collection of cytoplasmic and nuclear histograms for SW480 cells. (e) Ensemble collection of cytoplasmic and nuclear histograms for SW620 cells.

response to obtain the sample-specific reflectance $R(\lambda, x, y)$. To avoid system noise, only the spectral fluctuations between the wavelength range of 500 to 700 nm were analyzed. The statistical properties of the spectrum are used to determine the organizational properties of the refractive index of the specimen quantified through the disorder strength. A disorder strength map is determined from the spectral image cube [Fig. 4(b)]. Details about the theory, validation, and step-wise calculations of L_d are reported in the supplementary information of Ref. 19.

The physical basis of PWS is described in detail in Refs. 10, 37, 38, and 39. Briefly, PWS is based on the optical interference of backscattered light waves that are sensitive to the spatial

variations of optical refractive index at subdiffraction length scales.^{10,37,39} As refractive index is a linear function of local macromolecular mass density (DNA, RNA, proteins, etc.), PWS quantifies the nanoscale refractive index fluctuations, and thus, spatial fluctuations in macromolecular density, through a parameter called disorder strength L_d . Hence, biologically, disorder strength measures the macromolecular compaction within a cell. Theoretically, $L_d = \delta n^\alpha \times l_c^\beta$, where δn is the standard deviation of the refractive index variations, and l_c is the correlation length of these variations. In a cell, δn is defined by the inhomogeneity of macromolecular density and l_c is the characteristic size of the intracellular structures. The exponent

Table 1 Description of each NIQPM-based density metric determined in cytoplasmic and nuclear compartments.

Physical property	Unit	Description
Area	μm^2	Area of cellular compartment
Total dry mass	pg	Sum of dry mass density in compartment
Mean dry mass density, μ	$\text{pg}/\mu\text{m}^2$	Average value of dry mass in compartment
Standard deviation of density, σ	$\text{pg}/\mu\text{m}^2$	Mean variation of density about the mean
Coefficient of variation	—	Ratio of mean and standard deviation
Mode	$\text{pg}/\mu\text{m}^2$	Most common value of density
Median	$\text{pg}/\mu\text{m}^2$	Density value separating low and high
Max density	$\text{pg}/\mu\text{m}^2$	Maximum observed compartmental density
Min density	$\text{pg}/\mu\text{m}^2$	Minimum observed compartmental density
Skew	—	Measure of asymmetry of density distribution
Kurtosis	—	Measure of peakedness of density distribution

α depends on the refractive index contrast of the medium on top of a cell relative to its internal fluctuations (i.e., the cytology sample preparation) and is equal to 1 in our case, while β depends on the configuration of the optical setup (i.e., collection numerical aperture of the system) and is ~ 1 for the instrumentation used in this study. All the disorder strength values are calculated for the nuclear region of each cell. The nuclear region is determined from the reflection-mode bright field images.

2.5 Statistical Analysis

For NIQPM studies, the Jarque–Bera test was used to evaluate normality of all parameters. One-way analysis of variance with Bonferonni *post hoc* correction was used to assess statistical significance among parameters across multiple normally distributed cell parameters. The Kruskal–Wallis test was used to assess significance among non-normally distributed parameters. *P* values of 0.05 or less were considered significant. Correlations among parameters were determined using the 0th lag of the normalized covariance. Statistical significance of correlations was determined using standard Student’s *t*-tests. All NIQPM-based density quantities are presented as mean \pm standard error.

For PWS studies, the mean disorder strength is calculated after averaging the two-dimensional map of $L_d(x, y)$ [where (x, y) is the pixel location] over the selected region of interest [e.g., nucleus, Fig. 4(b)]. This average value is denoted by $L_d(x, y)$, and the standard deviation of intracellular disorder strength values were also calculated. The averages of $L_d(x, y)$ over a group of cells, 50 to 70 per cell type, are termed as the “group mean” of the disorder strength and denoted $L_d^{(g)}$; the standard deviation of this quantity is denoted $\sigma_d^{(g)}$. The group mean, $L_d^{(g)}$, along with its standard error calculated over all the cells, is depicted in all bar graphs of disorder strength in this study. *P* values were calculated using standard Student’s *t*-tests assuming unequal variances. The % fold-increase (mean difference) between the two cell types was used as the differentiating parameter. The percent difference was considered significant for *P* values less than 0.05.

3 Results

3.1 Validation of a Model System of Metastatic Transition in CRC Cell Types

Carcinogenesis requires the stepwise accumulation of genetic and epigenetic alterations in cells over the time scale of years. Structural alterations downstream of these events detectable by conventional histological studies, employing diffraction limited light microscopy that probe length scales ≥ 250 nm, represent the final stages of the cancerization process. We have previously established that architectural consequences occurring at the 20- to 200-nm scale during earlier stages of carcinogenesis, in which genetic/epigenetic aberrations have occurred, precede histological changes, and can be optically quantified through the nuclear disorder strength measured by PWS.¹⁰ Specifically, PWS has quantified differences among microscopically similar looking cells in genetically altered colon cancer cell lines and in the cells obtained from the AOM (azoxymethane treated) rat model and the multiple neoplasia mouse model.¹⁰ Furthermore, PWS has detected increasing nuclear disorder strength among cells in clinical samples obtained from histologically normal mucosa as a function of decreasing distance from colon, lung, ovarian, and pancreatic cancer lesions.^{12,19,20} Together, these studies demonstrate that higher nuclear disorder strength in cells is positively correlated with higher tumorigenic potential.

In the current study, the patient-matched SW620 (lymph node metastasis, late stage) and SW480 (primary colon adenocarcinoma, early stage) CRC cell lines were selected to provide an isogenic system of metastasis. To establish a model of architectural changes associated with early steps in the metastatic cascade, we characterized the nuclear disorder strength of morphologically similar SW480 and SW620 cell types (Figs. 2 and 4).

We verified that the CRC cells possess differing tumorigenic potentials as quantified by the nuclear disorder strength. Fifty cells from each CRC cell type were measured. The nuclear disorder strength of SW620 cells was found to be statistically

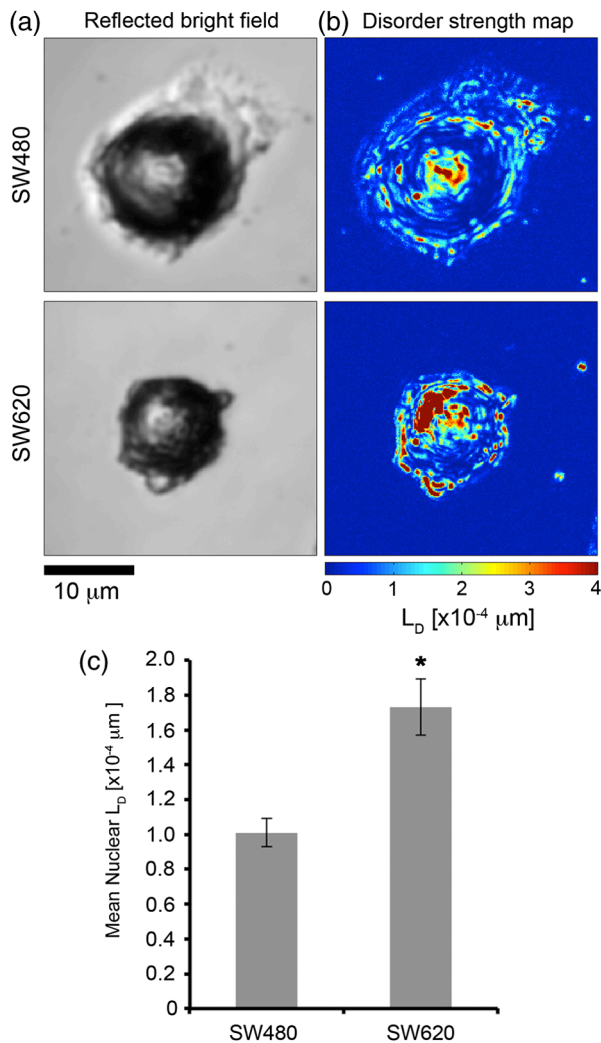


Fig. 4 Nanoscale disorder strength measurement of SW cell types using PWS. (a) Reflection-mode bright field images of SW480 and SW620 cells obtained with the PWS system. (b) Disorder strength maps of SW cell types. (c) Bar graph depicting mean nuclear disorder strength measurements among 50 cells of each SW cell type. * denotes $P < 0.05$ with respect to SW480 cells.

increased in comparison to SW480 cells, with a percent difference of 80% and P value of 2.85×10^{-5} [Fig. 4(c)]. The presence of these nanoscale architectural changes is an indicator of increased tumorigenic potential among the SW620 cells.

3.2 Differential Organization of Cytoplasmic and Nuclear Density in CRC Cell Types

A key question to understanding the physical basis of metastasis is how cellular mass is organized among nuclear and cytoplasmic domains as tumorigenic potential increases. To examine biophysical alterations as a function of tumorigenic potential, we quantified density organization across nuclear and cytoplasmic regions using NIQPM-based density measurements obtained from through-focus bright field imagery. Compartmental analysis of each cell was performed (Fig. 3) from which we quantified and compared 11 total parameters (Table 1) in both the cytoplasmic and nuclear regions (Fig. 5).

Histopathology of cancer at the cellular level has revealed that cells contributing to the pathogenesis of cancer possess increased nuclear area relative to cytoplasmic area. To verify that our model of early-stage disease recapitulated this hallmark of clinical identification, we quantified the area of the cytoplasmic and nuclear regions of each cell type. We observed that morphologically similar SW480 cells possessed an average nuclear area accounting for 35% of the total cell area, whereas in SW620 cells, the nucleus accounted for 51% of the total area (Fig. 5). These observed increases in the percentage of cell area that is nuclear in character supports this basic histopathological tenet of cancer and serves as further evidence to validate our model of carcinogenesis.

Total dry mass in the nucleus was increased with respect to the cytoplasm in both cell types. Although the cytoplasmic area of SW480 cells accounted for over half (64%) of the total area of SW480 cells, the total dry mass content of the nucleus of these cells surpassed the dry mass content of the cytoplasm. In comparing the total dry mass content of each compartment across cell type, the SW620 cells, whose nuclear area accounted for just over half of the total cell area, possessed a 1.8-fold increase in nuclear dry mass content compared to the cytoplasm. This finding would suggest that the SW620 cells are converging on a more dense organization, yet when mean dry mass was determined in each cellular compartment, a statistically similar cytoplasmic and nuclear dry mass density was observed (Fig. 5). We remark that the median and mode of the dry mass density distributions did not vary significantly from the mean density across both cell compartment and cell type.

Investigation of the standard deviation of the dry mass density in each compartment revealed that the cytoplasm of both CRC cell types varies more widely than the nucleus (Fig. 5). As an example, the cytoplasmic dry mass density histogram of a typical cell from each SW cell type is wider than the corresponding nuclear histogram [Figs. 3(b) and 3(c)]. This is further illustrated in the ensemble of probability density functions generated for each cell type [Figs. 3(d) and (e)]. Moreover, the nuclear standard deviation and the coefficient of variation were both increased 1.4-fold in SW620 cells in comparison to SW480 cells. These findings indicate that the uniformity of the nucleus, quantified by the variation of the density about the mean, is reduced in postmetastatic CRC cells.

To further characterize shape changes of the density distribution in each cell as a function of tumorigenic potential, we computed the skew and kurtosis of the distributions. Skew is a measure of distributional asymmetry in which positive skew indicates that the histogram leans more toward the origin, whereas a negative skew indicates that the distribution leans toward density values greater than the mean. A skew of zero is symmetric about the mean. The Kurtosis quantifies peak shape of a probability distribution with extremes being “thin” (kurtosis > 0.5) or “broad” (kurtosis < 0.5) peaks. For example, the normal distribution has a kurtosis of 0.5.

The cytoplasm of SW480 cells possessed the only significantly distinct skews, found to be positive, whereas the nuclear and cytoplasmic skews of the SW620 cells were statistically indistinguishable from a symmetric distribution (Fig. 5). We observed that the kurtosis of the dry mass density was broad although the kurtosis of the cytoplasm was broader than the nuclear regions. This finding reinforces our earlier observation of increased standard deviation and the coefficient of variation of the dry mass density distributions of the cytoplasm in

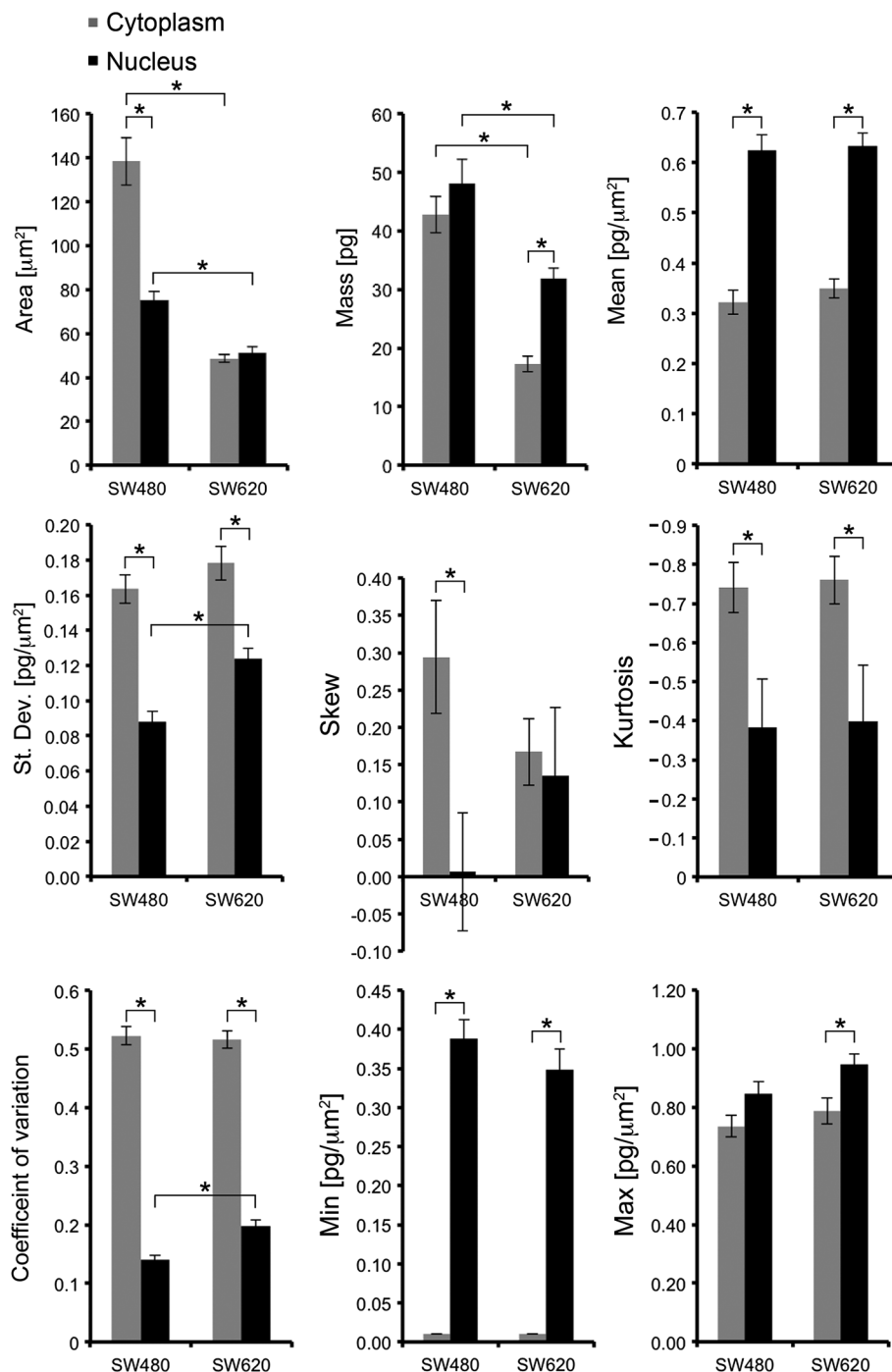


Fig. 5 Dry mass density metrics comparisons across cellular compartments and CRC SW cell types.

both CRC cell types. We note that the kurtosis of the cytoplasm and nucleus of each CRC cell type were statistically indistinguishable.

Next, we quantified the minimum and maximum observed density values measured in each cellular compartment. Minimum cytoplasmic measurements were found to correspond to the noise-floor of the NIQPM method. This indicates that both cell types possess thin membrane protrusions that cannot be further quantified with our diffraction-limited approach. The corresponding minimum nuclear density observed was not statistically distinguishable across cell type. When comparing the maximum densities observed across SW480 cell compartments,

a similar value was obtained (Fig. 5). We investigated the origin of these dense cytoplasmic features in SW480 cells and found that these values corresponded to pixels in the density map spatially located near the nuclear envelope [Fig. 2(b), arrows]. The maximum nuclear density was distinct from the maximum cytoplasmic density in SW620 cells although this metric was not statistically distinct across cell type.

Having conducted a micron-level analysis of cellular density using both the total dry mass in each compartment and an array of statistical and shape parameters of the dry mass density distribution, we observe that only a subset of the 11 parameters are distinct across SW cell types. These include nuclear area,

nuclear/cytoplasmic mass, nuclear dry mass density standard deviation, and dry mass density coefficient of variation. These parameters are presumably being regulated downstream with the (dis)organization of cellular density at the nanoscale, as quantified by PWS, and provide a corresponding micron-scale characterization of cellular architectural changes associated with metastasis.

3.3 Interdependence of Micron-Scale Subcellular Density Metrics: Network Signatures of Density Metrics

Our investigation of cellular density metrics at the micron level revealed that only 4 of the 11 density metrics demonstrated utility in differentiating SW480 cells from SW620 cells. Although these findings indicate that some micron-level density metrics are conserved among pre and postmetastatic CRC cells, we examined the potential role of interdependent relationships among these quantities in specifying quantitative signatures of disease stage in this model system.

To elucidate potential coupling among biophysical metrics, we computed population-wide correlation coefficients between parameters describing the same compartment, e.g., comparing nuclear area with nuclear skew and across cellular compartments, e.g., comparing cytoplasmic mass and nuclear area. Correlations that were not statistically significant were set to zero.

The collection of these parameter correlations defines a network of interdependencies between nodes representing the different measured dry mass density metrics. Linkages among

nodes are determined by the value of the correlation coefficient between the two measured parameters. We present these networks in terms of a heat map representing the correlation structure to provide a simple means of comparison (Fig. 6). Each correlation coefficient was placed in a matrix and then represented as a heat map ranging from blue (anti-correlation of -1) to white (zero correlation) to red (correlation of $+1$). The top row of Fig. 6 corresponds to networks for cytoplasmic autocorrelation [Fig. 6(a)], nuclear autocorrelation [Fig. 6(b)], and cytoplasmic-nuclear cross-correlations in SW480 cells [Fig. 6(c)]. The middle row (Figs. 6(d)–6(f)) presents the same networks for SW620 cells. The final row [Figs. 6(g)–6(i)] presents the result of subtracting the SW620 correlation map from the SW480 map for each of the different types of compartmental analyses.

Inspection of the correlation difference maps reveals that the “nuclear-nuclear” network [Fig. 6(h)] of interdependencies is more conserved across cell type in comparison to the “cytoplasmic-cytoplasmic” difference map [Fig. 6(g)]. Interestingly, while the nuclei of the SW480 and SW620 cells possessed statistically distinct areas, dry mass content, as well as density standard deviation and coefficient of variation; the corresponding network of interdependencies of these quantities was conserved across cell type for all but dry mass and area [Fig. 6(h)]. Among density metrics that were significantly altered in the cytoplasm across cell type i.e., area and mass, both of these quantities were drastically different in their level of interconnectedness when comparing SW480 and SW620 cells [Fig. 6(g)].

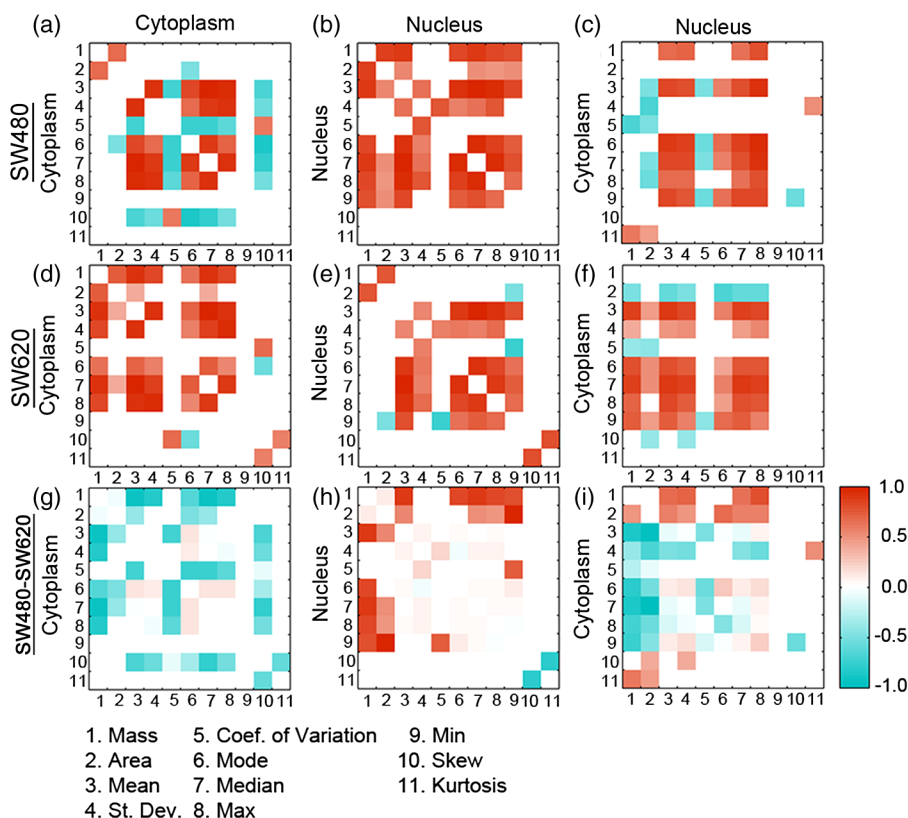


Fig. 6 Correlative studies of density metric interdependencies. (a–c) SW480 correlations among cytoplasmic-specific, nuclear-specific, and cytoplasmic-nuclear quantities. (d–f) SW620 correlations among cytoplasmic-specific, nuclear-specific, and cytoplasmic-nuclear quantities. (g–i) Differences between SW480 and SW620 maps computed by subtracting SW620 correlation maps from SW480 correlation maps. Numbers encode different quantities as listed in the key.

To quantify features specific to each network, we first determined the importance of the nodes in the network by enumerating the total number of connections each node possessed [Fig. 7(a)–7(c)]. We then assessed the uniqueness of network features to cell compartment and cell type by quantifying the percentage of the total connections each node possessed that were independent [Fig. 7(b)–7(f)]. Connections were considered “the same” if the correlation between two parameters was both statistically significant and of the same sign.

As an example, in the cytoplasmic-cytoplasmic network for SW480 cells [Fig. 6(a)], cytoplasmic mass (row or column 1) has only one connection, i.e., to cell area. By contrast, the cytoplasmic-cytoplasmic network for SW620 cells [Fig. 6(b)] possesses six connections between cytoplasmic mass and other cytoplasmic density parameters. This fact is presented in Fig. 7(a) under “Mass.” We then investigated the total number of cytoplasmic-cytoplasmic connections that cell mass possesses that are distinct from the corresponding connections present in cytoplasmic-cytoplasmic network of SW480 cells. The answer in this example is 5 out of 6 or 83%. This finding is presented in Fig. 7(d) under “Mass.” Note that 0% of the SW480 cytoplasmic mass connections was distinct in this case, as SW620 cells possessed a positive correlation to cytoplasmic area as well. Using these measures of nodal importance and connection independence, we investigated the relationships of the 11 density metrics as a function of metastatic potential.

A casual inspection of the number of network connections for each parameter [Figs. 7(a)–7(c)] demonstrates similar connectivity for many metrics; however, the level of independence of these connections is dynamic across cell type within each

network [Figs. 7(d)–7(f)]. A notable example is the differential role of mass among the cytoplasmic and nuclear networks. In the cytoplasmic network, the SW480 mass has no independent connections, whereas the SW620 mass has over 80% independence among its six connections. The situation is reversed in the nuclear network, in which SW620 mass now has 0 independent connections and SW480 mass connections are in excess of 80% independence with similarly reversed values of the number of connections. This scenario is observed for the coefficient of variation as well.

In examining the roles of density metrics that were significantly altered across cell type, 4 of the total 11 metrics were found to exhibit no independent connections within networks comparing interdependence of quantities in the same cellular compartment [Figs. 7(d) and 7(e)]. These included cytoplasmic mass and nuclear coefficient of variation among SW480 cells and nuclear area and nuclear mass among SW620 cells. Among nuclear density parameters that were not significantly altered when comparing cellular compartments across cell type, including the density mean, mode, median, kurtosis, and max; the nuclear network independence of these parameters was 0% among all these parameters [Fig. 7(e)] among SW620 cells. The mean, median, and mode did, however, possess unique roles in the cytoplasmic network and the cytoplasmic-nuclear network while the kurtosis played no independent role in any of the networks. Last, we remark that the skew shape parameter was most prominent in comparing cytoplasmic density [Figs. 7(a) and 7(d)].

The network structure of the density parameters demonstrates that while the %-independence may be similar for a given metric across cell type, a non-zero %-independence

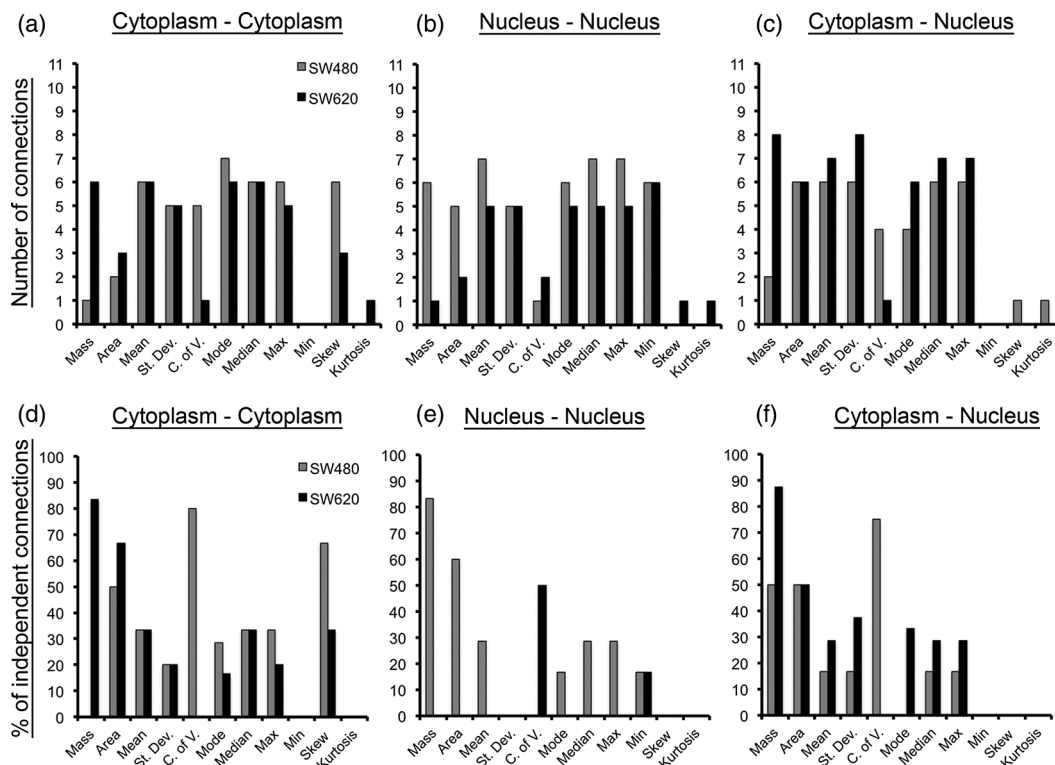


Fig. 7 Characterization of network topological properties: nodal connections and connection independence. Number of network connections among (a) cytoplasmic-cytoplasmic correlations, (b) nuclear-nuclear correlations, (c) cytoplasmic-nuclear correlations. % of independent connections among network connections among (d) cytoplasmic-cytoplasmic correlations, (e) nuclear-nuclear correlations, (f) cytoplasmic-nuclear correlations.

indicates a unique role for that parameter within the network. These distinct parametric network states for each cell type indicate a differential regulation of each facet of architecture in response to differing tumorigenic potentials. These findings suggest that while biophysical metrics of cells may or may not change in response to increased tumorigenic potential, the level of network interdependence to other quantities may provide additional insight into architectural changes associated with metastasis. Together, these results highlight an important role of density alterations at the micron level that are not revealed when only comparing shifts in individual parameters.

4 Discussion

In this work, we investigated the alteration and interdependence of subcellular density metrics in an isogenic *in vitro* model of pre and postmetastatic CRC. By utilizing quantitative optical microscopy techniques that probe both nanoscale and micron-scale density alterations in conjunction with image segmentation, we quantified the differential organization of cellular density in cytoplasmic and nuclear compartments. We examined the interdependence of 11 density metrics across cellular compartments and across cell types to investigate the dynamical interdependence of cellular density metrics during pre and postmetastatic cancer.

We observed that at the nanometer scale, SW620 cells possessed increased nuclear disorder strength in comparison to SW480 cells. At the micrometer scale, SW620 cells possessed increased nuclear density variations, increased nuclear coefficient of variation, increased nuclear to cytoplasmic ratio, increased nuclear to cytoplasmic mass ratio, and decreased nuclear and cytoplasmic area. SW480 and SW620 cells possess distinct physical parameter network topologies whose interdependencies consist of nodes of varying importance and whose connections highlight independent relationships among the architectural parameters defining the pre and postmetastatic phenotype.

Technological barriers currently prevent the simultaneous measurement of disorder strength using PWS and micrometer-scale density using NIQPM. The lack of an instrument that unifies these measurements has constrained our present study to the investigation of cells from the same passage. The goal of our future work will be to perform PWS- and NIQPM-based measurements on the same cells to provide a multiscale biophysical characterization of pre and postmetastatic cancer in terms of both changes in measured quantities and an examination of nuclear/cytoplasmic metric interdependence. Longitudinal investigation of cellular metrics in cell lines and clinical samples could enable the establishment of a mathematical model of cellular architecture underlying pre and post metastatic phenotypes.

5 Conclusion

As a constitutive equation relating density metrics to one another as a function of tumorigenic potential remains to be established, the network analysis approach utilized in this study provides an alternative strategy to quantify cellular structure through a mosaic of parameters and their interdependence. Though we give up deterministic knowledge of the cell, we can elucidate the differential regulation of mass density metrics to obtain an unbiased quantitative characterization of cellular architecture. Expanded studies using a combined PWS-NIQPM approach across cell line models of different cancers and the

investigation of patient samples will continue to define the utility of this network approach. In conclusion, multiscale optical measurement of subcellular density metrics across cellular compartments reveals not only shifts in density parameters in response to metastatic transitions in cancer, but also alterations of parameter interdependence.

Acknowledgments

This work was supported by the National Institutes of Health under grant nos. U54CA143906 (O.J.T.M., K.G.P.), U54CA143869, R01CA128641, R01CA165309 (D.D., V.B., H.S.); a Physical Sciences in Oncology Young Investigator Award (D.D., H.S., K.G.P.); and a Medical Research Foundation Early Clinical Investigator Award (K.G.P.). D.D. wishes to thank Varun Gupta for assistance with PWS measurements.

References

1. A. Jemal et al., "Cancer Statistics," *Cancer J. Clin.* **59**, 225–249 (2009).
2. J. E. Allen and W. S. El-Deiry, "Circulating tumor cells in colorectal," *Cancer. Curr. Colorectal Cancer Rep.* **6**, 212–220 (2010).
3. F. Michor et al., "What does physics have to do with cancer?," *Nat. Rev. Cancer* **11**, 657–670 (2011).
4. J. R. Mourant et al., "Spectroscopic diagnosis of bladder cancer with elastic light scattering," *Lasers Surg. Med.* **17**(4), 350–357 (1995).
5. R. S. Gurjar et al., "Imaging human epithelial properties with polarized light scattering spectroscopy," *Nat. Med.* **7**(11), 1245–1248 (2001).
6. A. Wax et al., "Cellular organization and substructure measured using angle-resolved low-coherence interferometry," *Biophys. J.* **82**, 2256–2264 (2002).
7. N. Terry et al., "Detection of intestinal dysplasia using angle-resolved low coherence interferometry," *J. Biomed. Opt.* **16**(10), 106002 (2011).
8. A. S. Haka et al., "Diagnosing breast cancer by using Raman spectroscopy," *Proc. Natl. Acad. Sci. U. S. A.* **102**, 12371–12376 (2005).
9. K. Chen et al., "Diagnosis of colorectal cancer using Raman spectroscopy of laser-trapped single living epithelial cells," *Opt. Lett.* **31**(13), 2015–2017 (2006).
10. A. Cerussi et al., "Predicting response to breast cancer neoadjuvant chemotherapy using diffuse optical spectroscopy," *Proc. Natl. Acad. Sci. U. S. A.* **104**, 4014–4019 (2007).
11. H. Subramanian et al., "Optical methodology for detecting histologically unapparent nanoscale consequences of genetic alterations in biological cells," *Proc. Natl. Acad. Sci. U. S. A.* **105**, 20118–20123 (2008).
12. D. Damania et al., "Nanocytology of rectal colonocytes to assess risk of colon cancer based on field cancerization," *Cancer Res.* **72**(11), 2720–2727 (2012).
13. Y. L. Kim et al., "Low-coherent backscattering spectroscopy for tissue characterization," *Appl. Opt.* **44**(3), 366–377 (2005).
14. Z. Wang et al., "Tissue refractive index as a marker of disease," *J. Biomed. Opt.* **16**(11), 116017 (2011).
15. R. K. Bista et al., "Nuclear nano-morphology markers of histologically normal cells detect the "field effect" of breast cancer," *Breast Cancer Res. Treat.* **135**(1), 115–124 (2012).
16. Y. Bishitz et al., "Optical-mechanical signatures of cancer cells based on fluctuation profiles measured by interferometry," *J. Biophotonics* (2013).
17. K. G. Phillips et al., "Optical quantification of cellular mass, volume, and density of circulating tumor cells identified in an ovarian cancer patient," *Front. Oncol.* **2**, 1–8 (2012).
18. H. K. Roy et al., "Association between rectal optical signatures and colonic neoplasia: potential applications for screening," *Cancer Res.* **69**, 4476–4483 (2009).
19. D. Damania et al., "Insights into the field carcinogenesis of ovarian cancer based on the nanocytology of endocervical and endometrial epithelial cells," *Int. J. Cancer* **133**(5), 1143–1152 (2013).
20. H. Subramanian et al., "Nanoscale cellular changes in field carcinogenesis detected by partial wave spectroscopy," *Cancer Res.* **69**(13), 5357–5363 (2009).

21. D. B. Agus et al., "A physical sciences network characterization of non-tumorigenic and metastatic cells," *Sci. Rep.* **3**, 1449 (2013).
22. A. Leibovitz et al., "Classification of human colorectal adenocarcinoma cell lines," *Cancer Res.* **36**, 4562–4569 (1976).
23. R. E. Hewitt et al., "Validation of a model of colon cancer progression," *J. Pathol.* **192**(4), 446–454 (2000).
24. H. V. Pham et al., "Real time blood testing using quantitative phase imaging," *PLoS One* **8**(2), e55676 (2013).
25. P. Girshovitz and N. T. Shaked, "Generalized cell morphological parameters based upon interferometric phase microscopy and their application to cell life cycle characterization," *Biomed. Opt. Express* **3**(8), 1757–1773 (2012).
26. J. Frank, S. Altmeyer, and G. Wernicke, "Non-interferometric, non-iterative phase retrieval by Green's functions," *J. Opt. Soc. Am. A* **27**, 2244–2251 (2010).
27. D. Paganin and K. A. Nugent, "Noninterferometric phase imaging with partially coherent light," *Phys. Rev. Lett.* **80**, 2586–2589 (1998).
28. K. G. Phillips, S. L. Jacques, and O. J. McCarty, "Measurement of single cell refractive index, dry mass, volume, and density using a transillumination microscope," *Phys. Rev. Lett.* **109**, 118105 (2012).
29. K.G. Phillips et al., "Quantification of cellular volume and sub-cellular density fluctuations: comparison of normal blood cells and breast cancer associated circulating tumor cells," *Front. Oncol.* **2**, 1–10 (2012).
30. S. M. Baker, K. G. Phillips, and O. J. McCarty, "Development of a label-free imaging technique for the quantification of thrombus formation," *Cell. Mol. Bioeng.* **5**(4), 488–492 (2012).
31. R. Barer, "Interference microscopy and mass determination," *Nature* **169**, 366–367 (1952).
32. G. Popescu, "Quantitative phase imaging of nanoscale cell structure and dynamics," in *Methods in Cell Biology*, B. Jena, Ed., Vol. 90, pp. 87–115, Elsevier, USA (2008).
33. M. Mir et al., "Optical measurement of cycle-dependent cell growth," *Proc. Natl. Acad. Sci. U. S. A.* **108**, 13124–13129 (2011).
34. J. Frank et al., "Refractive index determination of transparent samples by noniterative phase retrieval," *Appl. Opt.* **50**(4), 427–433 (2011).
35. C. Preza et al., "Phase imaging microscopy: beyond dark-field, phase contrast, and differential interference contrast microscopy," in *Handbook of Biomedical Optics*, pp. 483–517, D. Boas, C. Pitris, and N. Ramanujam, Eds., Taylor and Francis Books, Boca Raton, Florida (2012).
36. D. Damania et al., "The role of cytoskeleton in controlling the disorder strength of cellular nanoscale architecture," *Biophys. J.* **99**, 989–996 (2010).
37. P. Pradhan and N. Kumar, "Localization of light in coherently amplifying random-media," *Phys. Rev. B* **50**(13), 9644–9647 (1994).
38. Y. Stypula et al., "Understanding biological mechanisms of nuclear disorder strength in early carcinogenesis," *Gastroenterology* **140**(5), S765–S766 (2011).
39. L. Cherkezyan et al., "Interferometric spectroscopy of scattered light can quantify the statistics of subdiffractive refractive-index fluctuations," *Phys. Rev. Lett.* **111**, 033903 (2013).

Biographies of the authors are not available.